



# The Early Radio Afterglow of Short GRB 230217A

G. E. Anderson<sup>1</sup> , G. Schroeder<sup>2</sup> , A. J. van der Horst<sup>3</sup> , L. Rhodes<sup>4</sup> , A. Rowlinson<sup>5,6</sup> , A. Bahramian<sup>1</sup> , S. I. Chastain<sup>7</sup> ,  
B. P. Gompertz<sup>8</sup> , P. J. Hancock<sup>1,9</sup> , T. Laskar<sup>10</sup> , J. K. Leung<sup>11,12,13</sup> , and R. A. M. J. Wijers<sup>5</sup>

<sup>1</sup> International Centre for Radio Astronomy Research, Curtin University, GPO Box U1987, Perth, WA 6845, Australia; [gemma.anderson@curtin.edu.au](mailto:gemma.anderson@curtin.edu.au)

<sup>2</sup> Center for Interdisciplinary Exploration and Research in Astrophysics and Department of Physics and Astronomy, Northwestern University, 2145 Sheridan Road, Evanston, IL 60208-3112, USA

<sup>3</sup> Department of Physics, George Washington University, 725 21st St NW, Washington, DC 20052, USA

<sup>4</sup> Astrophysics, Department of Physics, University of Oxford, Keble Road, Oxford, OX1 3RH, UK

<sup>5</sup> Anton Pannekoek Institute for Astronomy, University of Amsterdam, Science Park 904, P.O. Box 94249, 1090GE Amsterdam, The Netherlands

<sup>6</sup> ASTRON, the Netherlands Institute for Radio Astronomy, Postbus 2, NL-7990 AA Dwingeloo, The Netherlands

<sup>7</sup> Department of Physics and Astronomy, University of New Mexico, 210 Yale Blvd NE, Albuquerque, NM 87106, USA

<sup>8</sup> Institute of Gravitational Wave Astronomy and School of Physics and Astronomy, University of Birmingham, Birmingham B15 2TT, UK

<sup>9</sup> Curtin Institute for Data Science, Curtin University, GPO Box U1987, Perth, WA 6845, Australia

<sup>10</sup> Department of Physics & Astronomy, University of Utah, Salt Lake City, UT 84112, USA

<sup>11</sup> David A. Dunlap Department of Astronomy and Astrophysics, University of Toronto, 50 St. George Street, Toronto, ON M5S 3H4, Canada

<sup>12</sup> Dunlap Institute for Astronomy and Astrophysics, University of Toronto, 50 St. George St., Toronto, ON M5S 3H4, Canada

<sup>13</sup> Racah Institute of Physics, The Hebrew University of Jerusalem, Jerusalem, 91904, Israel

Received 2024 September 2; revised 2024 October 4; accepted 2024 October 11; published 2024 October 28

## Abstract

We present the radio afterglow of short gamma-ray burst (GRB) 230217A, which was detected less than 1 day after the gamma-ray prompt emission with the Australia Telescope Compact Array (ATCA) and the Karl G. Jansky Very Large Array. The ATCA rapid-response system automatically triggered an observation of GRB 230217A following its detection by the Neil Gehrels Swift Observatory and began observing the event just 32 minutes postburst at 5.5 and 9 GHz for 7 hr. Dividing the 7 hr observation into three time-binned images allowed us to obtain radio detections with logarithmic central times of 1, 2.8, and 5.2 hr postburst, the first of which represents the earliest radio detection of any GRB to date. The decline of the light curve is consistent with reverse shock emission if the observing bands are below the spectral peak and not affected by synchrotron self-absorption. This makes GRB 230217A the fifth short GRB (SGRB) with radio detections attributed to a reverse shock at early times (<1 day postburst). Following brightness temperature arguments, we have used our early radio detections to place the highest minimum Lorentz factor ( $\Gamma_{\min} > 50$  at  $\sim 1$  hr) constraints on a GRB in the radio band. Our results demonstrate the importance of rapid radio follow-up observations with long integrations and good sensitivity for detecting the fast-evolving radio emission from SGRBs and probing their reverse shocks.

*Unified Astronomy Thesaurus concepts:* [Gamma-ray bursts \(629\)](#); [Radio transient sources \(2008\)](#)

## 1. Introduction

Binary neutron star (BNS) mergers are the key to understanding the behavior of nuclear matter at extreme densities (P. D. Lasky et al. 2014; V. Ravi & P. D. Lasky 2014; B. P. Abbott et al. 2018) and are likely the creation sites of the heaviest elements in the Universe (E. Pian et al. 2017; A. J. Levan et al. 2024). Short-duration gamma-ray bursts (GRBs) have long been thought to arise from BNS mergers (J. M. Lattimer & D. N. Schramm 1976; D. Eichler et al. 1989; R. Narayan et al. 1992; R. Mochkovitch et al. 1993), with the near-simultaneous detection of gravitational wave (GW) event GW170817 and GRB 170817A conclusively establishing this link (B. P. Abbott et al. 2017). Short GRBs (SGRBs) are classified based on their prompt gamma-ray emission lasting <2 s and being spectrally hard, while the other main class are long GRBs, which last >2 s and are spectrally soft (C. Kouveliotou et al. 1993). This emission arises from highly collimated relativistic jets driven by a black hole or rapidly spinning neutron star from the BNS merger (M. J. Rees & P. Meszaros 1992; M. Ackermann et al. 2010; L. Rezzolla et al. 2011). SGRBs only represent  $\sim 10\%$ – $20\%$  of the well-localized

GRB population discovered by instruments such as the Neil Gehrels Swift Observatory (hereafter Swift; N. Gehrels et al. 2004) Burst Alert Telescope (BAT; S. D. Barthelmy et al. 2005), making them quite rare with  $\lesssim 10$  detected per year with Swift.

The jet launched during an SGRB can result in a multi-wavelength afterglow, as predicted by the fireball model (M. J. Rees & P. Meszaros 1992; S. Kobayashi et al. 1997; R. Sari & T. Piran 1997; T. Piran 1999; S. Kobayashi & R. Sari 2000). In this model, the relativistic ejecta interacts with the circumburst medium (CBM), producing a forward shock that accelerates electrons and generates synchrotron emission detectable from radio to X-ray (and sometimes high-energy gamma-ray) wavelengths or energies from days to years postburst. A reverse shock is also generated, which propagates back into the shocked ejecta and can be detected as a distinct and much faster-evolving synchrotron component. This rapid evolution means that the reverse shock usually fades below detectability at X-ray and optical wavelengths within a few minutes (e.g., the optical reverse shock detection <90 s postburst from the possibly short duration GRB 180418A; R. L. Becerra et al. 2019), making the radio band the most viable option for detecting and tracking its evolution (e.g., A. J. van der Horst et al. 2014; J. S. Bright et al. 2023).

Radio observations are crucial to broadband modeling, which can map the afterglow flux density to the physical parameters of the explosion, such as its energetics and

magnetic field strength as well as the density and profile of the CBM (J. Granot & R. Sari 2002). Currently, only 17 SGRBs have been detected in the radio band (not including GW170817; E. Berger et al. 2005; A. M. Soderberg et al. 2006; W. Fong et al. 2014, 2015; G. P. Lamb et al. 2019; E. Troja et al. 2019; W. Fong et al. 2021; T. Laskar et al. 2022; G. E. Anderson et al. 2023b; L. Rhodes et al. 2023; S. I. Chastain et al. 2024; G. Schroeder et al. 2024a, 2024b), representing  $\sim 13\%$  of the full SGRB population with X-ray afterglows (G. Schroeder et al. 2024a). However, G. Schroeder et al. (2024a) showed that if only those events detected following the Karl G. Jansky Very Large Array (VLA) upgrade are considered (the instrument from which most detections are made) the detected fraction is much higher at  $\sim 34\%$ , illustrating the importance of sensitivity for detecting SGRB radio afterglows.

Of this sample of 17 SGRBs, 11 were detected in the radio band within 1 day postburst between 4 and 10 GHz and in several cases within a few hours. Interestingly, 8 events had faded below detectability by the time of their second or third observation between 4 and 9 days postburst. This indicates that  $\sim 50\%$  of the radio-detected SGRB population may fade within a few days postburst in the observer frame. Meanwhile, 6 SGRBs have shown radio emission beyond 10 days postburst, including GRB 211106A and GRB 230205A that were detected up to  $\sim 100$  days (T. Laskar et al. 2022; G. Schroeder et al. 2024a). Of these, GRB 210726A is unusual as it went undetected until 11.2 days postburst, at which point a radio flare lasting 50 days was detected with both MeerKAT and VLA, the likely explanation being late-time energy injection or a reverse shock from a shell collision (G. Schroeder et al. 2024b).

The low number of radio-detected SGRBs may be due to the observed short radio afterglow lifetime, as seen from  $\sim 50\%$  of the detected population. This rapid evolution indicates there should be significant variability on minute-to-hour timescales from reverse shock emission or scintillation that is likely missed by the  $\sim 1$  hr duration snapshot observations often obtained in the radio band (W. Fong et al. 2015; G. Schroeder et al. 2024a). To ensure radio detections and comprehensive modeling of the radio afterglow, we require rapid follow-up with observations lasting for several hours postburst.

To increase the number of radio-detected SGRBs and probe the early-time radio parameters space, we initiated a follow-up program using the Australia Telescope Compact Array (ATCA) in 2018 that utilizes the rapid-response triggering system (G. E. Anderson et al. 2021). When an SGRB is detected by Swift-BAT, the rapid-response system automatically observes the event as soon as it is above the horizon, provided it is at a decl.  $< +20$  deg (with an exclusion zone of  $-5 < \text{decl.} < +5$  deg necessary for east-west arrays). This ensures an observation occurs  $< 1$  day postburst, with integrations up to 12 hr. We then continue to observe the GRB three or four more times, which are logarithmically spaced in time, up to  $\sim 20$  days postburst. The first ATCA rapid-response observation was of SGRB 181123B, which began 12.6 hr postburst when the source had risen above the horizon (G. E. Anderson et al. 2021). A further four events were triggered as part of this program between 2020 and 2022, three of which were observed  $< 1$  day postburst with three additional observations in the following  $\sim 2$  weeks, all resulting in nondetections. These observations were combined with quasi-simultaneous observations performed by the South African

Square Kilometer Array precursor MeerKAT telescope, which enabled tight constraints to be placed on the gamma-ray efficiency and environmental density of eight SGRBs (S. I. Chastain et al. 2024).

Here we present the first ATCA rapid-response radio detection of an SGRB. ATCA began observing GRB 230217A just 32 minutes postburst for 7 hr, resulting in the earliest radio detection of any GRB to date. Further observations with ATCA and the VLA tracked the rapid decline of this radio emission, which faded below detectability between 5 and 10 GHz in less than 2 days postburst. In the following, we describe our observations and processing in Section 2 and radio analysis in Section 3. The GRB 230217A radio afterglow is then interpreted in the context of the SGRB population with radio detections  $< 1$  day postburst in Section 4. Throughout this Letter, we use the following power-law representation for flux density  $S \propto t^\alpha \nu^\beta$  and assume a cosmology of  $H_0 = 67.4$  and  $\Omega_m = 0.315$  (Planck Collaboration et al. 2020).

## 2. Observations and Results

The SGRB 230217A was initially reported by both the Swift-BAT and the Fermi Gamma-ray Space Telescope Gamma-ray Burst Monitor (C. Meegan et al. 2009) at 21:53:10 UT on 2023 February 17 (Fermi GBM Team et al. 2023; M. J. Moss et al. 2023). The Swift X-ray Telescope (XRT; D. N. Burrows et al. 2005) identified the X-ray afterglow (M. Capalbi et al. 2023a, 2023b). Unfortunately, the majority of XRT data were unreliable, thus preventing a robust analysis of the X-ray light-curve properties,<sup>14</sup> which is likely due to a Swift Moon constraint (M. J. Moss et al. 2023) and the delay in identifying its X-ray afterglow (M. Capalbi et al. 2023a, 2023b). The optical afterglow was also very faint (J. Gillanders et al. 2023; B. O’Connor & E. Troja 2023; Swift/BAT trigger et al. 2023), with only a single detection reported with magnitude  $I \sim 24.5$  at 2.5 days (P. D’Avanzo et al. 2023). The radio afterglow was detected with both ATCA (G. E. Anderson et al. 2023b) and the VLA (G. Schroeder et al. 2024a)  $< 1$  day postburst and marginally detected in a single MeerKAT observation at 5 days (S. I. Chastain et al. 2024). The data processing and results of the ATCA and VLA observations are described in the following sections.

### 2.1. ATCA

On receiving the trigger request following the Swift-BAT detection of GRB 230217A, ATCA was on target at 2023 February 17 22:21:25 UT, just 32 minutes postburst for 7 hr centered at the Swift-BAT position. Follow-up observations were also obtained at 1.2, 7, and 17 days postburst under program C3204 (PI Anderson). All ATCA observations were taken with a 6 km maximum baseline configuration using the 4 cm dual receiver with central frequencies of 5.5 and 9 GHz, each with a 2 GHz bandwidth. The flux and phase calibrators were PKS 1934-638 and PKS 1830-210, respectively, and the data were processed with MIRIAD using standard techniques (R. J. Sault et al. 1995). Each image was primary beam corrected. The flux densities were measured using the MIRIAD task `imfit`. We fitted a point source at the VLA position of the GRB (G. Schroeder et al. 2023) to obtain a force-fitted flux density measurement for those observations with no detection.

<sup>14</sup> [https://www.swift.ac.uk/xrt\\_curves/01154967/](https://www.swift.ac.uk/xrt_curves/01154967/) (P. A. Evans et al. 2007, 2009).

**Table 1**  
Flux Density Measurements of GRB 230217A

Telescope	Time <sup>a</sup> (days)	Exposure <sup>b</sup> (hr)	Frequency (GHz)	Flux Density ( $\mu$ Jy per beam)	$3\sigma$ Threshold <sup>c</sup> ( $\mu$ Jy per beam)	Frequency (GHz)	Flux Density ( $\mu$ Jy per beam)	$3\sigma$ Threshold <sup>c</sup> ( $\mu$ Jy per beam)
ATCA	0.08	7.1	5.5	<b>137 <math>\pm</math> 27</b>	51	9.0	<b>125 <math>\pm</math> 19</b>	39
	0.04 <sup>d</sup>	1.7	5.5	<b>96 <math>\pm</math> 27</b>	75	9.0	<b>152 <math>\pm</math> 30</b>	57
	0.12 <sup>d</sup>	1.5	5.5	<b>75 <math>\pm</math> 26</b>	68	9.0	<b>132 <math>\pm</math> 34</b>	65
	0.22 <sup>d</sup>	4.0	5.5	<b>163 <math>\pm</math> 43</b>	86	...	...	...
	1.22	3.0	5.5	<b>136 <math>\pm</math> 47</b>	109	9.0	47 $\pm$ 72	102
	6.93	7.4	5.5	18 $\pm$ 14	36	9.0	29 $\pm$ 13	31
	17.05	3.6	5.5	23 $\pm$ 30	51	9.0	24 $\pm$ 36	56
VLA	0.79	0.6	6.0	<b>70 <math>\pm</math> 9</b>	15	...	...	...
	0.776 <sup>e</sup>	0.15	6.0	<b>72 <math>\pm</math> 10</b>	21	...	...	...
	0.783 <sup>e</sup>	0.15	6.0	<b>50 <math>\pm</math> 11</b>	24	...	...	...
	0.789 <sup>e</sup>	0.15	6.0	<b>71 <math>\pm</math> 12</b>	26	...	...	...
	0.796 <sup>e</sup>	0.15	6.0	<b>67 <math>\pm</math> 13</b>	27	...	...	...
	21.74	0.4	6.0	24 $\pm$ 33	21	...	...	...

**Notes.** The flux densities in bold are detections ( $>3\sigma$ ). All those not bolded are nondetections ( $<3\sigma$ ) and are derived from force-fitting the clean Gaussian beam at the VLA position of the GRB (G. Schroeder et al. 2023).

<sup>a</sup> The central logarithmic time of the observation with respect to the Swift-BAT detection time of GRB 230217A.

<sup>b</sup> The total exposure of the images used to derive the flux density.

<sup>c</sup> The  $3\sigma$  threshold is the image rms multiplied by 3, which is used as an upper limit in Figure 1 for all nondetections.

<sup>d</sup> Flux densities derived from splitting the first ATCA observation into three and two images at 5.5 and 9 GHz, respectively.

<sup>e</sup> Flux density measurements from splitting the first VLA observation into four images of 9 minutes each.

The radio afterglow of GRB 230217A was detected in the rapid-response observations at both 5.5 and 9 GHz at the VLA position. As we expect the radio emission may experience variability on minute-to-hourly timescales  $<1$  day postburst, we split the observed into three images with total integrations of 1.5, 1.5, and 4 hr at 5.5 GHz and 1.5 and 1.5 hr at 9 GHz (the last 4 hr were not imageable at 9 GHz as the observing conditions had deteriorated). We also measured the average flux density from the full 7 hr image of the first ATCA observation. The afterglow was still detected at 5.5 GHz in a follow-up ATCA observation at 1.2 days postburst but had faded below detectable flux levels at 9 GHz. All further observations were nondetections. The  $1\sigma$  flux density errors for both the GRB and check source are the `imfit` statistical error added in quadrature to a 5% absolute flux density error, which is standard for ATCA. The GRB flux densities (including those measured from the split and average images of the first ATCA observation),  $1\sigma$  errors, and image rms near the GRB position are listed in Table 1, with the light curves at 5.5 and 9 GHz shown in Figure 1.

We also measured the flux density of a nearby uncatalogued radio source at R.A. = 18:42:50.54 ( $\pm 0''.02$ ) and decl. =  $-28:52:02.3$  ( $\pm 0''.06$ ) to test the absolute calibration between the ATCA and VLA observations. This source position was measured using the first VLA observation as it has a higher resolution than the ATCA observations (details of the VLA observations are in Section 2.2). The 5.5 GHz (and VLA 6 GHz) light curve of this check source is also plotted in Figure 1 as gray data points showing the flux densities are consistent within  $1-2\sigma$ .

## 2.2. VLA

Observations with the VLA were initiated on 2023 February 18 at 16:05:18 UT for 1 hr (36 minutes on target with midtime of 0.79 days postburst) at a mean frequency of 6 GHz (4 GHz bandwidth) under program 23A-296 (PI: Schroeder). Follow-

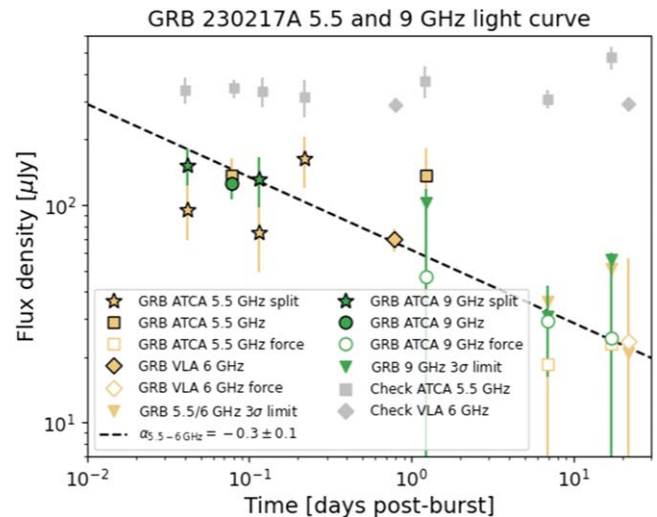


**Figure 1.** The radio light curve of GRB 230217A at 5.5 (ATCA observations; yellow squares/stars), 6 (VLA observations; yellow diamonds), and 9 GHz (ATCA observations; green circles/stars). The stars show the afterglow detections from splitting the first ATCA observation into three and two time-binned images at 5.5 and 9 GHz, respectively. The average flux density over the first ATCA observation and all subsequent ATCA observations are plotted as squares and circles at 5.5 and 9 GHz, respectively. The solid data points show detections ( $>3\sigma$ ), whereas the open data points are force-fitted flux densities at the known position of the GRB when there was no significant detection. For the nondetections, we also plot the  $3\sigma$  upper limits as downward pointing triangles. A nearby check source detected in all ATCA 5.5 GHz and VLA 6 GHz images is also plotted in gray to indicate the absolute flux density scale between the ATCA and VLA measurements. Overplotted is the power-law fit to the ATCA 5.5 GHz and VLA 6 GHz data using the average flux density from the first ATCA observation, as described in Section 3 and Table 2.

up observations were obtained at 21.74 days postburst. The flux calibrator was 3C286 and 3C48 for the first and second VLA observation, respectively, and J1820-2528 was used for the phase calibration of both observations. The observations were performed while the VLA was in B-configuration. The VLA

Science Ready Data Products produced by the Common Astronomy Software Applications (CASA; J. P. McMullin et al. 2007; I. M. van Bemmell et al. 2022) VLA Pipeline (CASA Pipeline Version 6.4.1.12) were downloaded, and the data were imaged using the VLA Imaging Pipeline<sup>15</sup> (version 2023.1.0.124, CASA version 6.5.4).

The flux densities of both the GRB and check source were measured from the primary beam corrected images using the MIRIAD task `imfit` to be consistent with the ATCA flux measurement process. A 5% absolute flux calibration error was added in quadrature to the statistical errors to produce the final  $1\sigma$  flux density errors, which is standard for the VLA. The VLA flux densities,  $1\sigma$  errors that include the 5% absolute flux calibration, and the image rms for GRB 230217A are listed in Table 1. The GRB and check source are plotted as yellow and gray diamonds in Figure 1, respectively. To test for short-term variability, we also split the first VLA observation into four images of 9 minutes each, with the resulting flux densities included in Table 1.

### 3. Radio Afterglow Analysis

The radio afterglow of GRB 230217A was detected up to 1.2 days postburst with ATCA and VLA in the 5.5–6 GHz radio band. Having split the ATCA rapid-response observation into three and two images at 5.5 and 9 GHz, respectively, the first flux density measurements have a logarithmic central time of 1 hr postburst (or 1.3 hr linear central time; see stars plotted in Figure 1), which is the earliest radio detection of any GRB to date.

We first investigate whether the flux density measurements of GRB 230217A could be affected by interstellar scintillation (ISS; J. Goodman 1997) as has been seen in the radio afterglows of several long GRBs (D. A. Frail et al. 1997; E. Waxman et al. 1998; D. A. Frail et al. 2000; P. Chandra et al. 2008; A. J. van der Horst et al. 2014; K. D. Alexander et al. 2019; L. Rhodes et al. 2022; G. E. Anderson et al. 2023a). The all-sky model for refractive interstellar scintillation (RISS19; P. J. Hancock et al. 2019) returns a transition frequency of  $\nu_0 = 8.9$  GHz, with a scattering screen distance of  $D = 1.3$  kpc, a scattering measure  $SM = 9 \pm 1 \times 10^{-4}$  kpc  $m^{-20/3}$ , and first Frenzel zone size of  $2.38 \mu\text{as}$  at  $\nu_0$ . This places our 5.5–6 GHz observations in the strong refractive regime and our 9 GHz observations near the transition frequency. Following the equations in Table 1 of J. Granot & A. J. van der Horst (2014), the predicted modulation index is up to  $m = 0.8$  and  $m = 1$  at 5.5 and 9 GHz, respectively, for GRB 230217A. The radio afterglow may also experience intrinsic variability due to the passage of characteristic frequencies in the afterglow-emitting region(s) (J. Granot & R. Sari 2002).

To test for evidence of short timescale variability within the first 1.2 days postburst, we performed a  $\chi^2$  test on the detections of GRB 230217A, returning a probability of  $P = 0.15$  that the radio afterglow is consistent with a steady source over this time frame (we require  $P < 0.001$  to claim variability, with  $0.01 < P < 0.001$  being undetermined; B. M. Gaensler & R. W. Hunstead 2000; M. E. Bell et al. 2015). A lack of detectable variability is not surprising given that splitting the first ATCA observation reduces the sensitivity and necessarily increases the size of the error bars. Similarly, we also perform a  $\chi^2$  test to search for intraobservational

**Table 2**  
The Temporal Index  $\alpha$  (Such That  $S \propto t^\alpha$ ) and Reduced  $\chi^2$  Statistic to a Single Power-law Fit to the 5.5–6 GHz Light-curve Data

$\nu$ (GHz)	First Observation <sup>a</sup>	$\alpha$	$\chi^2_{\text{red}}$
5.5–6	Split	$-0.2 \pm 0.1$	1.6
5.5–6	Average	$-0.3 \pm 0.1$	0.9

**Note.**

<sup>a</sup> Two fits were performed to the 5.5–6 GHz light curve using a single (Average) measurement or several (Split) measurements from the first ATCA observation (see Section 3).

variability within the first VLA observation when split into four  $\sim 9$  minute images, returning a probability of  $P = 0.5$  that the flux densities are consistent with a steady source within the 36 minute observation. While scintillation may affect the GRB radio afterglow, it is not significant enough to be distinguishable in our data set. Similarly, it is also not possible to ascertain if a characteristic frequency is evolving through the observing band within this  $\sim 1$  day time frame.

The same  $\chi^2$  test on the full 5.5–6 GHz GRB light curve, which includes the detections up to 1.2 days postburst and the force-fitted measurements for the nondetections at later times, returns a probability of  $P = 0.0016$  of being consistent with a steady source and thus a more likely indication of variability. This is also compared to  $P = 0.12$  derived from the 5.5 to 6 GHz measurements of the check source, which is therefore steady over the 22 days of monitoring.

The constraining  $3\sigma$  upper limits from the later observations (see Figure 1) demonstrate the overall radio light-curve trend of GRB 230217A is declining. We fit a single power law ( $S \propto t^\alpha$ ) to the 5.5–6 and 9 GHz light curves using SHERPA (P. Freeman et al. 2001). For both frequencies, we included the detections and force-fitted flux densities (the latter shown as open circles in Figure 1). At both frequencies, we performed two power-law fits to the light curve: one that included a single flux density measurement over the full integration of the first ATCA observation (“Average”) and the other using the flux densities measured from splitting this first observation into 3 and 2 images at 5.5 and 9 GHz, respectively (“Split”). The resulting power-law index and corresponding reduced  $\chi^2$  statistic for the two 5.5–6 GHz fits are listed in Table 2. The fits to the 9 GHz light curves failed as they resulted in an unphysical reduced  $\chi^2$  statistics near zero. We plot the power-law fit to the 5.5–6 GHz light curve that includes the average flux density from the first ATCA observation on Figure 1 where  $\alpha = -0.3 \pm 0.1$ , which we favor given its reduced  $\chi^2 \sim 1$ , and it is consistent with the  $3\sigma$  upper limit from the final VLA observation. Note that the faint GRB afterglow detections meant we could not derive meaningful information on the spectral index between 5.5 and 9 GHz.

### 4. Discussion

Given the limited multiwavelength data available for GRB 230217A (see Section 2), we restrict our investigation to just the radio afterglow. This includes an interpretation of the emission mechanism and a comparison to other early-time radio detections of SGRBs.

<sup>15</sup> <https://science.nrao.edu/facilities/vla/dataprocessing/pipeline/VIPL>

#### 4.1. Reverse Shock Emission

The overall trend of the 5.5 and 9 GHz light curve of GRB 230217A is declining with a temporal index of  $\alpha = -0.3 \pm 0.1$ . In Section 3, we demonstrate that our radio detections, which all occurred before 1.2 days postburst, do not provide significant evidence for scintillation and that a characteristic frequency such as the synchrotron self-absorption break moving through the observing bands cannot be distinguished.

We now examine the detected radio emission from GRB 230217A under the reverse–forward shock framework (P. Mészáros & M. J. Rees 1997). The forward and reverse shocks are both sites of particle acceleration where a population of electrons is accelerated into a power-law distribution of energies with a slope of  $p$ , generating two synchrotron components. The broadband spectrum of each component is described by the peak flux and three characteristic break frequencies (the synchrotron self-absorption frequency  $\nu_a$ , the peak frequency  $\nu_m$  and the cooling frequency  $\nu_c$ ), which evolve with time (J. Granot & R. Sari 2002). The evolution of these breaks depends on  $p$  and the slope  $k$  of the density profile  $\rho$  of the CBM as a function of radius  $R$  ( $\rho \propto R^{-k}$ ), where  $k=0$  corresponds to a homogeneous medium and  $k=2$  to a stellar wind-like medium. We assume that GRB 230217A is embedded within a homogeneous medium ( $k=0$ ), which is a standard assumption for SGRBs.

Analytical solutions of the temporal power-law indices of the flux density of the radio afterglow for both the forward and reverse shock can be found in Table 5 of A. J. van der Horst et al. (2014). On the timescales of our radio detections of GRB 230217A (hours to  $\sim 1$  day postburst), we expect the characteristic frequencies to be ordered  $\nu_a < \nu_m < \nu_c$  for both the forward and reverse shocks and that  $\nu$  is likely below  $\nu_m$  and either below or above  $\nu_a$  (J. Granot & A. J. van der Horst 2014). For radio emission from the forward shock to decay in this same time frame, we would require our observing frequency  $\nu > \nu_m$ . If this were the case then our temporal decay index implies  $p = 1.4 \pm 0.1$  for a homogeneous CBM. This is much lower than the range  $2 \lesssim p \lesssim 3$  expected for GRBs (R. Sari et al. 1999), making a forward shock interpretation unlikely.

Briefly exploring other forward shock interpretations, we note that the observed slope is also consistent with post-jet-break evolution when  $\nu_a < \nu < \nu_m$  (expected value of  $\alpha = -1/3$ ). However, this implies that a jet break occurred within the first hour after the gamma-ray trigger, which would be extremely early and imply a very narrow opening angle. We also note that the radio detections  $\lesssim 1$  day postburst are consistent with a flat light curve, which we expect for a forward shock when  $\nu_a < \nu < \nu_m$  and  $k=2$ . However, we disfavor this interpretation as we do not expect SGRBs to be embedded in wind-like environments.

The declining light curve better resembles reverse shock expectations, for which the  $\nu_a < \nu < \nu_m$  spectral regime predicts a temporal index in the range of  $-0.47 \lesssim \alpha \lesssim -0.45$  (depending on the thickness of the shell behind the forward shock through which the reverse shock must propagate; A. J. van der Horst et al. 2014) and is therefore consistent within  $2\sigma$  of our results. We rule out  $\nu < \nu_{a,m}$  as it predicts a rising light curve. It is also unlikely that  $\nu_a < \nu_m < \nu < \nu_c$  within the first  $\sim 1.2$  days postburst as this regime predicts much steeper temporal indices in the range of  $-2.7 < \alpha < -1.3$  in a homogeneous CBM for  $2 \leq p \leq 3$ , which accounts for

different shell thicknesses behind the forward shock. We therefore conclude we have detected radio emission from the reverse shock of GRB 230217A and that our observing bands ( $\nu$ ) are likely  $\nu_a < \nu < \nu_m$  within 1.2 days postburst.

GRB 230217A was marginally detected at 1.3 GHz with MeerKAT, measuring a flux density of  $23 \pm 5 \mu\text{Jy}$  at 5 days postburst. This observation was the first of five taken with MeerKAT between 5 and 156 days postburst (S. I. Chastain et al. 2024). Given that there is no clear forward shock component in the 5.5–6 and 9 GHz light curves, it is possible the MeerKAT detection was also of the reverse shock. If we interpret the rapid decline in the ATCA light curves as the reverse shock, then  $\nu_a$  is likely already below 5.5 and 9 GHz by the start of the first observation. Again following the relations presented in Table 5 of A. J. van der Horst et al. (2014),  $\nu_a$  evolves as  $t^{-0.53}$  for a thick-shell reverse shock with  $\nu_a < \nu_m < \nu_c$  and  $k=0$  (note this temporal slope is very similar to the thin-shell case, which is between  $-0.61 < \alpha < -0.54$ ). If we assume  $\nu_a \approx 9$  GHz just before our ATCA observations at  $\sim 1$  hr, we would expect  $\nu_a \approx 1.3$  GHz at  $\sim 2$  days. Provided the MeerKAT frequency remained in the  $\nu_a < \nu < \nu_m$  spectral regime up to 5 days postburst, then for an expected reverse shock decline of  $\alpha \sim -0.5$ , this suggests a peak flux density between 30 and 40  $\mu\text{Jy}$  at 1.3 GHz. It is therefore not unreasonable to suggest the marginal MeerKAT detection was from the fading reverse shock emission.

GRB 230217A is now the best-sampled radio reverse shock of an SGRB in the first hours postburst (see Section 4.2), due to the 7 hr ATCA observation beginning 32 minutes postburst that was combined with VLA and ATCA follow-up. However, the reduction in sensitivity caused by dividing the observation into smaller time bins (plus potential scintillation effects) makes it difficult to characterize the evolution of the reverse shock. For example, we cannot ascertain if  $\nu_a$  was evolving through the observing bands during our observations or if it was already below these frequencies by the start of the first ATCA observation. This demonstrates that sensitivity also plays an important role (along with rapid observations with long integrations) in characterizing the reverse shock emission.

#### 4.2. Comparison to Early-time Radio Detections of SGRBs

The radio light curves of GRB 230317A are compared to all the radio-detected SGRBs with observations between 5–8 and 8–10 GHz in Figure 2. Upper limits from observations of SGRBs not detected in these radio bands are also plotted (W. Fong et al. 2015; G. Schroeder et al. 2024a), including the five events observed with ATCA under this rapid-response program (C3204; G. E. Anderson et al. 2021; S. I. Chastain et al. 2024). Figure 2 showcases the ATCA rapid-response mode’s ability to probe timescales  $< 0.1$  days postburst, a previously unexplored regime, with GRB 230217A setting a new record in the earliest radio detection of a GRB.

As mentioned in Section 1, 11 of the radio bright SGRBs ( $\sim 65\%$ ) were detected  $< 1$  day postburst, with the majority fading below detectability within a week. Of these 11 SGRBs, multiwavelength modeling has attributed the  $< 1$  day radio emission of 4 events to the reverse shock (GRBs 051221A, 160821B, 200522A, and 231117A; A. M. Soderberg et al. 2006; G. P. Lamb et al. 2019; E. Troja et al. 2019; W. Fong et al. 2021; G. Schroeder et al. 2024a), but in each case only one or two data points sampled this synchrotron component. The light curves for these four GRBs are also highlighted in

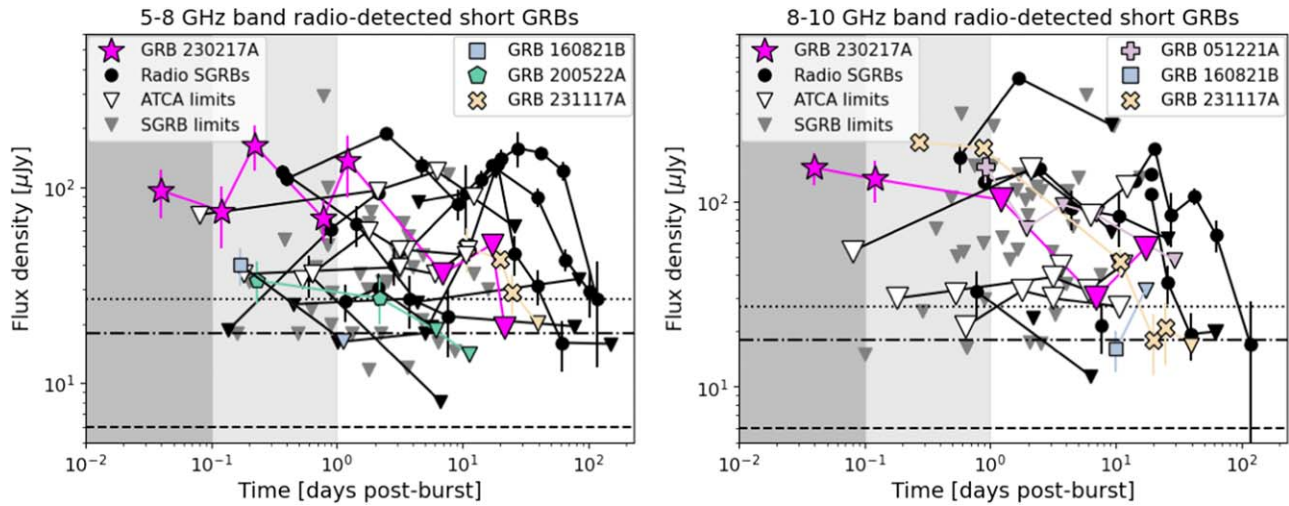


**Figure 2.** The light curves of SGRBs observed in the radio band between 5–8 (left) and 8–10 GHz (right). The magenta stars and triangles correspond to the detections and upper limits of GRB 230217A from Table 1. The other SGRBs with early-time ( $<1$  day postburst) radio emission attributed to a reverse shock from the jet hitting the CBM are also indicated with different colored symbols (A. M. Soderberg et al. 2006; G. P. Lamb et al. 2019; W. Fong et al. 2021; L. Rhodes et al. 2023; G. Schroeder et al. 2024a). The black data points correspond to the other 12 radio-detected SGRBs from the literature, with circles and triangles denoting detections and upper limits, respectively (E. Berger et al. 2005; W. Fong et al. 2014, 2015, 2021; T. Laskar et al. 2022; G. Schroeder et al. 2024a, 2024b; A. J. Levan et al. 2024). The gray triangles show upper limits of other SGRBs not detected in the radio band taken from W. Fong et al. (2015) and G. Schroeder et al. (2024a). The white triangles are upper limits from the ATCA SGRB-triggering program published in G. E. Anderson et al. (2021) and S. I. Chastain et al. (2024). The light-gray region indicates those SGRBs with detections within 1 day postburst, and the dark gray region illustrates times  $<0.1$  days postburst, which is a parameter space we can now probe using rapid-response observations. The horizontal dotted lines show the VLA  $3\sigma$  sensitivity for a 9 minute image. The horizontal dashed and dotted-dashed lines show the expected  $3\sigma$  sensitivity of a 9 and 1 minute image with the Square Kilometer Array Mid, respectively (see Section 5).

Figure 2 for direct comparison with GRB 230217A. Of the remaining SGRBs with detected radio emission  $<1$  day postburst, 3 are attributed to the forward shock (GRBs 050724A, 130603B, and 140903A; E. Berger et al. 2005; W. Fong et al. 2014, 2015; E. Troja et al. 2016), whereas the other 4 are unmodeled. This makes GRB 230217A the fifth SGRB with radio emission attributed to a reverse shock from the jet hitting the CBM, and it has the densest time sampling of this emission component.

#### 4.3. Minimum Lorentz Factor

Our early-time radio detections of GRB 230217A provide a unique opportunity to place the earliest radio constraints on the minimum Lorentz factor ( $\Gamma_{\min}$ ) of the outflow using brightness temperature arguments (T. J. Galama et al. 1999). Usually, minimum Lorentz factors are measured from the gamma-ray emission emitted during the prompt phase of the outburst with  $\Gamma_{\min} > 100$ –1000 (M. Ackermann et al. 2010). However, some important constraints have also been placed from rapid detections at other wavelengths (T. J. Galama et al. 1999). Due to the inverse squared dependence of brightness temperature on the observing frequency, early radio detections can place comparison constraints on  $\Gamma_{\min}$  derived from the opposite end of the spectrum. This type of analysis has been done for other (mainly long) GRBs that have radio detections  $\lesssim 1$  day postburst, with  $\Gamma_{\min} \sim 10$ –30 (G. E. Anderson et al. 2014, 2018). Meanwhile, the most constraining minimum Lorentz factors of  $\Gamma_{\min} \sim 20$ –35 were obtained from tracking the reverse shock evolution of the luminous long GRB 221009A that allowed for an equipartition analysis (J. S. Bright et al. 2023).

We calculated the brightness temperature  $T_b$  of GRB 230217A for all detections using Equation (1) from G. E. Anderson et al. (2014), which assumes a nonrelativistic flow such that the emission region size is simply the observing time  $t$  multiplied by

the speed of light. We then derived  $\Gamma_{\min}$  based on the rest-frame maximum brightness temperature in the inverse-Compton limit where  $T_B \approx 10^{12}$  K such that  $T_b/T_B = \Gamma^3$  (T. J. Galama et al. 1999). Assuming an average radio-detected SGRB redshift of  $z = 0.5$  for GRB 230217A (G. Schroeder et al. 2024a), we derived a minimum Lorentz factor of  $\Gamma_{\min} > 50$  and  $\Gamma_{\min} > 40$  from the earliest detection at  $\sim 1$  hr postburst at 5.5 and 9 GHz, respectively. We also derived  $\Gamma_{\min}$  for the radio SGRB population for all detections  $<2$  days postburst, which are plotted as a function of time in Figure 3. These are directly compared to  $\Gamma_{\min}$  from the ATCA and VLA detections of GRB 230217A, which are now the most constraining GRB limits derived from the radio band.

## 5. Conclusions

This analysis of GRB 230217A highlights the impact of the ATCA rapid-response program for GRB studies as it probes a previously unexplored radio parameter space of  $<0.1$  days and tracks the early afterglow evolution. Using the ATCA rapid-response mode, we observed the SGRB 230217A just 32 minutes postburst, obtaining the earliest radio detection of a GRB to date. Combined ATCA and VLA observations showed a fading radio light curve consistent with reverse shock emission. This makes GRB 230217A the fifth SGRB with radio detections attributed to a reverse shock at early times ( $<1$  day postburst). Using brightness temperature arguments, we have also placed the tightest constraint on the minimum Lorentz factor in the radio band of  $\Gamma_{\min} > 50$ , assuming an average radio-detected SGRB redshift of 0.5.

While rapid follow-up with long integrations is key for detecting SGRB radio reverse shocks, we have not tracked their frequency-dependent evolution, which is necessary for probing the thickness of the ejecta material, the density profile of the CBM, and the energetics of the outburst, as has been possible for a small number of long GRBs (e.g., J. S. Bright et al. 2023).

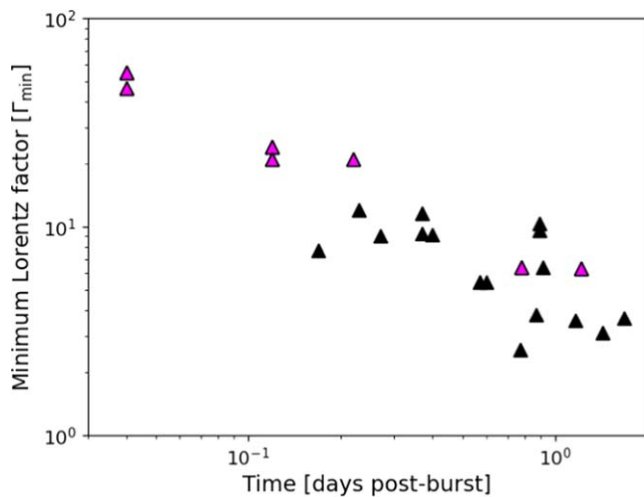


**Figure 3.** Lower limits on the minimum Lorentz factors probed by early-time ( $<2$  day postburst) radio detections of SGRBs as a function of time postburst (E. Berger et al. 2005; A. M. Soderberg et al. 2006; W. Fong et al. 2014, 2015, 2021; L. Rhodes et al. 2023; G. Schroeder et al. 2024a). GRB 230217A is plotted in magenta showing the most constraining limits obtained for SGRBs in the radio band.













This ATCA program already demonstrates the advantage of sensitivity and several-hour integrations over the previous GRB rapid-response program (T. D. Staley et al. 2013; G. E. Anderson et al. 2018) performed with the Arcminute Microkelvin Imager Large Array (J. T. L. Zwart et al. 2008), which pioneered this functionality for GRB science. These results encourage installing similar rapid-response programs on other sensitive radio telescopes. For example, a single 36 minute VLA observation can reach an rms of  $\sim 5 \mu\text{Jy beam}^{-1}$  (see Table 1), which was successfully split into four 9 minute images (see Section 3) with an rms of  $\sim 9 \mu\text{Jy beam}^{-1}$  (see the  $3\sigma$  limit drawn as dotted lines in Figure 2, which is expected to be similar for the C(4.0–8.0 GHz) and X(8.0–12.0 GHz) bands in the B array configuration<sup>16</sup>). Square Kilometer Array Mid is expected to reach an rms of  $\sim 2 \mu\text{Jy beam}^{-1}$  and  $\sim 6 \mu\text{Jy beam}^{-1}$  at the position of GRB 230217A in a 9 and 1 minute observation, respectively, assuming an elevation of 45 deg and a Briggs weighting scheme with Robust set to 0 in both the 4.6–8.5 and 8.3–15.4 GHz bands (see the  $3\sigma$  limits drawn as dashed and dotted–dashed lines in Figure 2).<sup>17</sup> A rapid-response trigger within 12 hr postburst that lasts for  $\gtrsim 3$  hr with either instrument would allow us to monitor the rapidly varying early-time radio emission on minute timescales with competitive sensitivity for deep and high-cadence tracking of short and long GRB reverse shocks.

### Acknowledgments

We acknowledge the Gomeroi people as the traditional owners of the Australia Telescope Compact Array (ATCA) observatory site. ATCA is part of the Australia Telescope National Facility, which is funded by the Australian Government for operation as a National Facility managed by CSIRO. We acknowledge the Whadjuk Nyungar people as the traditional owners of the land on which the Bentley Curtin University campus is located, where the majority of this research was conducted. We thank the referee for their

recommendations on improving this Letter. G.E.A. is the recipient of an Australian Research Council Discovery Early Career Researcher Award (project No. DE180100346) funded by the Australian Government. This research makes use of ASTROPY, a community-developed core Python package for Astronomy (Astropy Collaboration et al. 2018), NUMPY (S. van der Walt et al. 2011), and SCIPY (E. Jones et al. 2001) Python modules. This research also makes use of MATPLOTLIB (J. D. Hunter 2007). This research has made use of NASA’s Astrophysics Data System. This research has made use of SAOImage DS9, developed by the Smithsonian Astrophysical Observatory.

### ORCID iDs

G. E. Anderson  <https://orcid.org/0000-0001-6544-8007>  
 G. Schroeder  <https://orcid.org/0000-0001-9915-8147>  
 A. J. van der Horst  <https://orcid.org/0000-0001-9149-6707>  
 L. Rhodes  <https://orcid.org/0000-0003-2705-4941>  
 A. Rowlinson  <https://orcid.org/0000-0002-1195-7022>  
 A. Bahramian  <https://orcid.org/0000-0003-2506-6041>  
 S. I. Chastain  <https://orcid.org/0000-0003-3507-335X>  
 B. P. Gompertz  <https://orcid.org/0000-0002-5826-0548>  
 P. J. Hancock  <https://orcid.org/0000-0002-4203-2946>  
 T. Laskar  <https://orcid.org/0000-0003-1792-2338>  
 J. K. Leung  <https://orcid.org/0000-0002-9415-3766>  
 R. A. M. J. Wijers  <https://orcid.org/0000-0002-3101-1808>

### References

- Abbott, B. P., Abbott, R., Abbott, T. D., et al. 2017, *ApJL*, **848**, L13  
 Abbott, B. P., Abbott, R., Abbott, T. D., & Acernese 2018, *PhRvL*, **121**, 161101  
 Ackermann, M., Asano, K., Atwood, W. B., et al. 2010, *ApJ*, **716**, 1178  
 Alexander, K. D., Laskar, T., Berger, E., et al. 2019, *ApJ*, **870**, 67  
 Anderson, G. E., Bell, M. E., Stevens, J., et al. 2021, *MNRAS*, **503**, 4372  
 Anderson, G. E., Russell, T. D., Faushey, H. M., et al. 2023a, *MNRAS*, **523**, 4992  
 Anderson, G. E., Staley, T. D., van der Horst, A. J., et al. 2018, *MNRAS*, **473**, 1512  
 Anderson, G. E., Stevens, J., Bell, M. E., et al. 2023b, *GCN*, **33433**, 1  
 Anderson, G. E., van der Horst, A. J., Staley, T. D., et al. 2014, *MNRAS*, **440**, 2059  
 Astropy Collaboration, Price-Whelan, A. M., Sipőcz, B. M., et al. 2018, *AJ*, **156**, 123  
 Barthelmy, S. D., Barbier, L. M., Cummings, J. R., et al. 2005, *SSRv*, **120**, 143  
 Becerra, R. L., Dichiaro, S., Watson, A. M., et al. 2019, *ApJ*, **881**, 12  
 Bell, M. E., Huynh, M. T., Hancock, P., et al. 2015, *MNRAS*, **450**, 4221  
 Berger, E., Price, P. A., Cenko, S. B., et al. 2005, *Natur*, **438**, 988  
 Bright, J. S., Rhodes, L. L., Farah, W., et al. 2023, *NatAs*, **7**, 986  
 Burrows, D. N., Hill, J. E., Nousek, J. A., et al. 2005, *SSRv*, **120**, 165  
 Capalbi, M., Kennea, J. A., Tohuvavohu, A., et al. 2023a, *GCN*, **33348**, 1  
 Capalbi, M., Kennea, J. A., Tohuvavohu, A., et al. 2023b, *GCN*, **33365**, 1  
 Chandra, P., Cenko, S. B., Frail, D. A., et al. 2008, *ApJ*, **683**, 924  
 Chastain, S. I., van der Horst, A. J., Anderson, G. E., et al. 2024, *MNRAS*, **532**, 2820  
 D’Avanzo, P., Rossi, A., Brivio, R., et al. 2023, *GCN*, **33374**, 1  
 Eichler, D., Livio, M., Piran, T., & Schramm, D. N. 1989, *Natur*, **340**, 126  
 Evans, P. A., Beardmore, A. P., Page, K. L., et al. 2007, *A&A*, **469**, 379  
 Evans, P. A., Beardmore, A. P., Page, K. L., et al. 2009, *MNRAS*, **397**, 1177  
 Fermi GBM Team 2023, *GCN*, **33338**, 1  
 Fong, W., Berger, E., Margutti, R., & Zauderer, B. A. 2015, *ApJ*, **815**, 102  
 Fong, W., Berger, E., Metzger, B. D., et al. 2014, *ApJ*, **780**, 118  
 Fong, W., Laskar, T., Rastinejad, J., et al. 2021, *ApJ*, **906**, 127  
 Frail, D. A., Kulkarni, S. R., Nicastro, L., Feroci, M., & Taylor, G. B. 1997, *Natur*, **389**, 261  
 Frail, D. A., Kulkarni, S. R., Sari, R., et al. 2000, *ApJ*, **534**, 559  
 Freeman, P., Doe, S., & Siemiginowska, A. 2001, *Proc. SPIE*, **4477**, 76  
 Gaensler, B. M., & Hunstead, R. W. 2000, *PASA*, **17**, 72  
 Galama, T. J., Briggs, M. S., Wijers, R. A. M. J., et al. 1999, *Natur*, **398**, 394  
 Gehrels, N., Chincarini, G., Giommi, P., et al. 2004, *ApJ*, **611**, 1005

<sup>16</sup> <https://obs.vla.nrao.edu/ect/>

<sup>17</sup> <https://sensitivity-calculator.skao.int/mid>

- Gillanders, J., O'Connor, B., & Troja, E. 2023, *GCN*, **33368**, 1
- Goodman, J. 1997, *NewA*, **2**, 449
- Granot, J., & Sari, R. 2002, *ApJ*, **568**, 820
- Granot, J., & van der Horst, A. J. 2014, *PASA*, **31**, e008
- Hancock, P. J., Charlton, E. G., Macquart, J.-P., & Hurley-Walker, N. 2019, arXiv:1907.08395
- Hunter, J. D. 2007, *CSE*, **9**, 90
- Jones, E., Oliphant, T., Peterson, P., et al., 2001 SciPy: Open Source Scientific Tools for Python, v1.11.3, <https://www.scipy.org/>
- Kobayashi, S., Piran, T., & Sari, R. 1997, *ApJ*, **490**, 92
- Kobayashi, S., & Sari, R. 2000, *ApJ*, **542**, 819
- Kouveliotou, C., Meegan, C. A., Fishman, G. J., et al. 1993, *ApJL*, **413**, L101
- Lamb, G. P., Tanvir, N. R., Levan, A. J., et al. 2019, *ApJ*, **883**, 48
- Laskar, T., Escorial, A. R., Schroeder, G., et al. 2022, *ApJL*, **935**, L11
- Lasky, P. D., Haskell, B., Ravi, V., Howell, E. J., & Coward, D. M. 2014, *PhRvD*, **89**, 047302
- Lattimer, J. M., & Schramm, D. N. 1976, *ApJ*, **210**, 549
- Levan, A. J., Gompertz, B. P., Salafia, O. S., et al. 2024, *Natur*, **626**, 737
- McMullin, J. P., Waters, B., Schiebel, D., Young, W., & Golap, K. 2007, in ASP Conf. Ser. 376, *Astronomical Data Analysis Software and Systems XVI*, ed. R. A. Shaw, F. Hill, & D. J. Bell (San Francisco, CA: ASP), 127
- Meegan, C., Lichti, G., Bhat, P. N., et al. 2009, *ApJ*, **702**, 791
- Mészáros, P., & Rees, M. J. 1997, *ApJ*, **476**, 232
- Mochkovitch, R., Hernanz, M., Isern, J., & Martin, X. 1993, *Natur*, **361**, 236
- Moss, M. J., Eyles-Ferris, R. A. J., Gropp, J. D., et al. 2023, *GCN*, **33339**, 1
- Narayan, R., Paczynski, B., & Piran, T. 1992, *ApJL*, **395**, L83
- O'Connor, B., & Troja, E. 2023, *GCN*, **33356**, 1
- Pian, E., D'Avanzo, P., Benetti, S., et al. 2017, *Natur*, **551**, 67
- Piran, T. 1999, *PhR*, **314**, 575
- Planck Collaboration, Aghanim, N., Akrami, Y., et al. 2020, *A&A*, **641**, A6
- Ravi, V., & Lasky, P. D. 2014, *MNRAS*, **441**, 2433
- Rees, M. J., & Meszaros, P. 1992, *MNRAS*, **258**, 41
- Rezzolla, L., Giacomazzo, B., Baiotti, L., et al. 2011, *ApJL*, **732**, L6
- Rhodes, L., Anderson, G. E., van der Horst, A. J., et al. 2023, *GCN*, **35097**, 1
- Rhodes, L., van der Horst, A. J., Fender, R., et al. 2022, *MNRAS*, **513**, 1895
- Sari, R., & Piran, T. 1997, *MNRAS*, **287**, 110
- Sari, R., Piran, T., & Halpern, J. P. 1999, *ApJL*, **519**, L17
- Sault, R. J., Teuben, P. J., & Wright, M. C. H. 1995, in ASP Conf. Ser. 77, *Astronomical Data Analysis Software and Systems IV*, ed. R. A. Shaw, H. E. Payne, & J. J. E. Hayes (San Francisco, CA: ASP), 433
- Schroeder, G., Fong, W., Berger, E., & Laskar, T. 2023, *GCN*, **33358**, 1
- Schroeder, G., Fong, W.-f., Kilpatrick, C. D., et al. 2024a, arXiv:2407.13822
- Schroeder, G., Rhodes, L., Laskar, T., et al. 2024b, *ApJ*, **970**, 139
- Soderberg, A. M., Berger, E., Kasliwal, M., et al. 2006, *ApJ*, **650**, 261
- Staley, T. D., Titterton, D. J., Fender, R. P., et al. 2013, *MNRAS*, **428**, 3114
- Swift/BAT trigger 2023, *GCN*, **33370**, 1
- Troja, E., Castro-Tirado, A. J., Becerra González, J., et al. 2019, *MNRAS*, **489**, 2104
- Troja, E., Sakamoto, T., Cenko, S. B., et al. 2016, *ApJ*, **827**, 102
- van Bemmell, I. M., Kettenis, M., Small, D., et al. 2022, *PASP*, **134**, 114502
- van der Horst, A. J., Paragi, Z., de Bruyn, A. G., et al. 2014, *MNRAS*, **444**, 3151
- van der Walt, S., Colbert, S. C., & Varoquaux, G. 2011, *CSE*, **13**, 22
- Waxman, E., Kulkarni, S. R., & Frail, D. A. 1998, *ApJ*, **497**, 288
- Zwart, J. T. L., Barker, R. W., Biddulph, P., et al. 2008, *MNRAS*, **391**, 1545